



Disentangling Coexisting Structural Order Through Phase Lock-In Analysis of Atomic-Resolution STEM Data

Berit H. Goodge¹ , Ismail El Baggari^{2,†}, Seung Sae Hong^{3,4,‡}, Zhe Wang¹, Darrell G. Schlom^{5,6}, Harold Y. Hwang^{3,4} and Lena F. Kourkoutis^{1,6*} 

¹School of Applied and Engineering Physics, Cornell University, Ithaca, NY 14853, USA; ²Department of Physics, Cornell University, Ithaca, NY 14853, USA; ³Geballe Laboratory for Advanced Materials, Stanford University, Stanford, CA 94305, USA; ⁴Stanford Institute for Materials and Energy Sciences, SLAC National Accelerator Laboratory, Menlo Park, CA 94025, USA; ⁵Department of Materials Science and Engineering, Cornell University, Ithaca, NY 14853, USA and ⁶Kavli Institute at Cornell for Nanoscale Science, Cornell University, Ithaca, NY 14853, USA

Abstract

As a real-space technique, atomic-resolution STEM imaging contains both amplitude and geometric phase information about structural order in materials, with the latter encoding important information about local variations and heterogeneities present in crystalline lattices. Such phase information can be extracted using geometric phase analysis (GPA), a method which has generally focused on spatially mapping elastic strain. Here we demonstrate an alternative phase demodulation technique and its application to reveal complex structural phenomena in correlated quantum materials. As with other methods of image phase analysis, the phase lock-in approach can be implemented to extract detailed information about structural order and disorder, including dislocations and compound defects in crystals. Extending the application of this phase analysis to Fourier components that encode periodic modulations of the crystalline lattice, such as superlattice or secondary frequency peaks, we extract the behavior of multiple distinct order parameters within the same image, yielding insights into not only the crystalline heterogeneity but also subtle emergent order parameters such as antipolar displacements. When applied to atomic-resolution images spanning large ($\sim 0.5 \times 0.5 \mu\text{m}^2$) fields of view, this approach enables vivid visualizations of the spatial interplay between various structural orders in novel materials.

Key words: atomic resolution STEM, geometric phase analysis, heterogeneity, superlattice, quantum materials

(Received 30 August 2021; revised 12 January 2022; accepted 20 January 2022)

Introduction

Structurally and electronically complex materials may contain multiple coexisting lattice distortions which govern functional properties ranging from ferromagnetism and ferroelectricity to superconductivity (Ramesh & Spaldin, 2007). In complex oxides, for instance, the perovskite lattice may undergo distortions that underlie the diversity of electronic properties, including oxygen octahedral rotations (Catalano et al., 2018), cation antipolar distortions, and ferroelectric displacements (Ahn et al., 2004; Spaldin & Fiebig, 2005). Elastic strain variations and localized defects further enrich, or complicate, the structural landscape by modulating or disturbing the local structural ordering (Tokura & Hwang, 2008). This is particularly evident in modern material platforms, such as epitaxial thin films and multilayers or two-dimensional (2D) membranes, where defects, strain, and

structural responses conspire to create multiscale behavior and exotic electronic properties (Hong et al., 2020; Xu et al., 2020b). The complexity of oxides thus requires extracting quantitative structural information across length scales ranging from atomic to hundreds of nanometers.

Scanning transmission electron microscopy (STEM) that allows for direct imaging of atomic columns in materials has been widely adopted for detailed structural analysis. In particular, the imaging contrast of high-angle annular dark-field (HAADF)-STEM depends strongly on the atomic number and is suitable for robust structural quantification. When coupled with optimized data acquisition and analysis, HAADF-STEM also enables atomic position tracking with picometer precision (Yankovich et al., 2014; Nord et al., 2017) and compositional mapping with sub-Å resolution (LeBeau et al., 2008; Hwang et al., 2013; Kim et al., 2016). Such quantification provides a direct experimental measurement of exotic or functional material properties: for example, local polarization structures or elastic strain can be mapped in real space by determining the position of each atomic column in a material (Jia et al., 2007; Catalan et al., 2011; Nelson et al., 2011). Other imaging methods provide additional types of information at similar length scales: with annular bright-field (ABF)-STEM imaging or integrated differential phase contrast (iDPC) (Lazić et al., 2016), the role of bond

[†]Current address: Rowland Institute at Harvard, Cambridge, MA 02142, USA.

[‡]Current address: Department of Materials Science and Engineering, University of California Davis, Davis, CA 95616, USA.

*Corresponding author: Lena F. Kourkoutis, E-mail: lena.f.kourkoutis@cornell.edu

Cite this article: Goodge BH, El Baggari I, Hong SS, Wang Z, Schlom DG, Hwang HY, Kourkoutis LF (2022) Disentangling Coexisting Structural Order Through Phase Lock-In Analysis of Atomic-Resolution STEM Data. *Microsc Microanal* 28, 404–411. doi:10.1017/S1431927622000125

angles and octahedral rotations in complex oxides can be quantified as well (Findlay et al., 2009; Gao et al., 2016; Wang et al., 2016; Guo et al., 2017; Gao et al., 2018). Still, all of these techniques rely on the identification and fitting of all relevant atomic columns in data sets with high signal-to-noise ratios (SNR). Even with the highest-quality data, such analysis can be computationally tedious and intractable over very large fields of view. Moreover, multi-functional materials may contain multiple coexisting structural order parameters contributing to lattice distortions, making it difficult to disentangle or pinpoint the interplay between order parameters via direct real-space displacement mapping techniques (Savitzky et al., 2017).

Fourier-based methods are an attractive alternative to analyze structural information without the need for isolating individual atomic columns and obtaining over-sampled, high SNR data. They also naturally disentangle structural orders with different periodicities. Geometric phase analysis (GPA) (Hýtch et al., 2003; Rouviere & Sarigiannidou, 2005) is a leading method for analyzing elastic strain in materials by extracting deformations of a crystalline lattice relative to a chosen reference. This is especially useful for mapping the strain fields around defects (e.g., dislocations) or relaxation of epitaxial strain in thin films (Hýtch et al., 2003; Chu et al., 2004; Catalan et al., 2011; Zhu et al., 2013; Han et al., 2018).

There have been, however, notable limitations to conventional applications of geometric phase analysis techniques to STEM and high-resolution TEM images. Many complex materials of fundamental and technological interest, such as charge-ordered systems and (anti)ferroelectrics, exhibit additional structural modulations that lower the symmetry of the underlying crystalline lattice to form superlattices. Even in materials with superlattice order, most studies have generally focused on extracting strain in the primary crystalline lattice (Loudon et al., 2007; Zheng et al., 2018; Liao et al., 2019; Fan et al., 2020), without directly addressing the microscopic behavior of the superlattice. Given the demonstrated value and versatility of such image phase analysis techniques, it follows that their extension to additional signals and corresponding order parameters promises to unlock rich information about modulations in correlated materials.

Here, we present an alternative implementation of phase analysis based on principles of lock-in processing (Lawler et al., 2010; Mesaros et al., 2011). This phase lock-in method is mathematically related to GPA (Hýtch & Gandais, 1995) except that it performs the phase demodulation in real space rather than reciprocal space, yielding qualitatively and conceptually identical results. With this approach, we show how harnessing different periodicities of atomic-resolution STEM images can be used to disentangle defects and spatial modulations in not just crystalline but also superlattice order. Applying this technique to atomic-resolution STEM data, we demonstrate the ability to map coexisting structural order parameters over large fields of view. By extracting phase information beyond conventional strain, novel insights into complex structural order and disorder are revealed, including the observation of distinct variations in the atomic lattice versus emergent structural order parameters. The approach presented here can be similarly implemented within existing and widely accessible GPA frameworks for broad applications throughout materials science.

Methods

The SrTiO₃ shown in Figure 2 was grown using molecular beam epitaxy as a thin film on crystalline Si, as described in Wang et al.

(2019). A plan-view sample was prepared by back-polishing using the tripod technique (Voyles et al., 2003) followed by 10° and 8° ion milling at 3 kV and 1 kV, respectively, with a Fischione 1010 Ion Mill to reduce the effects of surface damage. The (La,Ca)MnO₃ film shown in Figures 1, 3, and 4 was grown by pulsed laser deposition on a water-soluble buffer layer and delaminated to produce a free-standing oxide membrane using the method described in Lu et al. (2016) and Hong et al. (2020). We note that the sample imaged and shown in this work was prepared prior to the completion of growth optimization and should therefore not be considered structurally representative of the samples discussed in those published reports. Once released from the growth substrate, the 20 nm thick oxide membrane was transferred to a TEM grid with holes (Quantifoil) for large-area plan-view imaging.

STEM imaging was performed on an aberration-corrected FEI Titan Themis microscope operating at 300 kV with 50 pA probe current and a convergence angle of 21 or 30 mrad. HAADF-STEM images shown in Figures 1–3 used inner and outer collection angles of 68 and 200 mrad, respectively. The annular dark-field (ADF) image shown in Figure 4 includes more diffraction contrast due to the inclusion of lower scattering angles down to 40 mrad. This collection geometry is a consequence of the instrumental set-up and should have little effect on the resulting analysis.

As with all real-space analyses of scanned images, care must be taken to limit the introduction of artifacts through image distortions from mechanical or other instabilities such as sample drift. The images shown in Figures 1 and 3 are obtained by aligning and averaging rapidly acquired image frames using rigid registration (Savitzky et al., 2018) to increase the image SNR and mitigate effects from instabilities. The images shown in Figures 2 and 4 are acquired as single image scans without any external or additional drift correction, though great care was taken in both the instrument environment and during the experiment to reduce the presence and impact of mechanical noise. Additional strategies to mitigate the possibility of artifacts were employed, including relatively fast scan speeds (~1 μs per pixel dwell time) and scan rotations chosen to minimize the effect of scan distortions along the direction of the periodicity of interest.

Theory

The intensity of an atomic-resolution image, $I(\mathbf{r})$, can be described by its Fourier decomposition

$$I(\mathbf{r}) = \sum_{\mathbf{k}} I_{\mathbf{k}}(\mathbf{r}) \exp [i(\mathbf{k} \cdot \mathbf{r} + \phi_{\mathbf{k}}(\mathbf{r}))], \quad (1)$$

where \mathbf{r} is the position vector, $I_{\mathbf{k}}$ is the Fourier amplitude, \mathbf{k} is the reciprocal lattice vector, and $\phi_{\mathbf{k}}(\mathbf{r})$ is the geometric phase encoding the deviations (such as strain) from the set of atomic lattice fringes associated with a particular \mathbf{k} -vector, \mathbf{Q} .

In the GPA method, extracting $\phi_{\mathbf{k}}(\mathbf{r})$ associated with a Bragg vector \mathbf{Q} is performed by first applying a mask, such as a two-dimensional Gaussian, around \mathbf{Q} in the fast Fourier transform (FFT). Performing an inverse Fourier transform and taking the argument of the complex-valued result yields the raw phase (Hýtch et al., 2003)

$$\psi_{\mathbf{Q}}(\mathbf{r}) = \mathbf{Q} \cdot \mathbf{r} + \phi_{\mathbf{Q}}(\mathbf{r}). \quad (2)$$

The geometric phase image is thus obtained by subtracting a reference $\mathbf{Q} \cdot \mathbf{r}$, i.e., $\phi_{\mathbf{Q}}(\mathbf{r}) = \psi_{\mathbf{Q}}(\mathbf{r}) - \mathbf{Q} \cdot \mathbf{r}$.

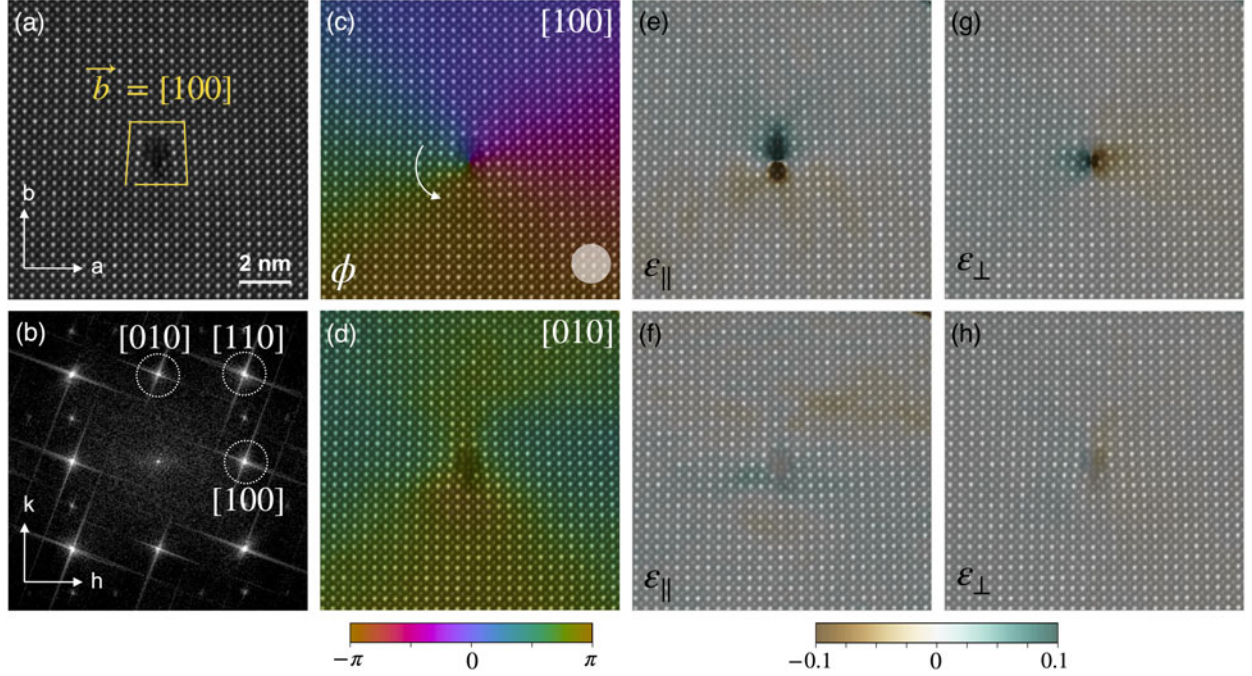


Fig. 1. A simple edge dislocation in a (La,Ca)MnO₃ membrane shows a perfect 2π phase winding when \mathbf{k} is along the direction of the Burgers vector. (a) HAADF-STEM lattice image and (b) FFT with the pseudocubic (reciprocal) lattice vectors labeled according to the convention used here. The size of the Gaussian mask used for phase lock-in analysis (dotted circles) is chosen for a corresponding real-space resolution of 1.5 nm. (c,d) Phase maps generated by the lock-in analysis of the [100] and [010] Bragg peaks, respectively. The phase of the [100] lattice fringes winds by 2π around the dislocation. (e-h) Transverse (ε_{\perp}) and longitudinal (ε_{\parallel}) strain maps generated from the gradients of the corresponding phase maps. “Dumbbell”-shaped singularities in the lattice strain are visible for the [100] fringes, while the orthogonal [010] fringes show very little strain effects. The circle in (c) shows the real-space coarsening length of the lock-in analysis in all maps. Phase and strain maps in (c-h) are overlaid on the original HAADF-STEM image in (a) for clarity of comparison; raw phase and strain maps are provided in Supplementary Figure S2.

In the phase lock-in method for an arbitrary wavevector \mathbf{k} , we mask the contributions of the \mathbf{k} -point and its symmetric reflection, $-\mathbf{k}$, which yields the local periodic amplitude

$$A_{\mathbf{k}}(\mathbf{r}) = 2|I_{\mathbf{k}}(\mathbf{r})| \cos(\mathbf{k} \cdot \mathbf{r} + \phi_{\mathbf{k}}) \quad (3)$$

Note that this amplitude will be identical for the treatment of both $+\mathbf{k}$ and $-\mathbf{k}$ (Hýtch et al., 1998). To extract the phase for a specific wavevector $+\mathbf{k}$, we apply the lock-in approach (Lawler et al., 2010; Mesaros et al., 2011) by multiplying the amplitude signal by two reference signals $\cos(\mathbf{k} \cdot \mathbf{r})$ and $\sin(\mathbf{k} \cdot \mathbf{r})$ to get components $X(\mathbf{r})$ and $Y(\mathbf{r})$ where

$$\begin{aligned} X(\mathbf{r}) &= 2|I_{\mathbf{k}}(\mathbf{r})| \cos(\mathbf{k} \cdot \mathbf{r} + \phi_{\mathbf{k}}) \cos(\mathbf{k} \cdot \mathbf{r}) \\ Y(\mathbf{r}) &= 2|I_{\mathbf{k}}(\mathbf{r})| \cos(\mathbf{k} \cdot \mathbf{r} + \phi_{\mathbf{k}}) \sin(\mathbf{k} \cdot \mathbf{r}) \end{aligned} \quad (4)$$

Using trigonometric relations, we obtain

$$\begin{aligned} X(\mathbf{r}) &= |I_{\mathbf{k}}(\mathbf{r})| (\cos \phi_{\mathbf{k}}(\mathbf{r}) + \cos(2\mathbf{k} \cdot \mathbf{r} + \phi_{\mathbf{k}}(\mathbf{r}))) \\ Y(\mathbf{r}) &= |I_{\mathbf{k}}(\mathbf{r})| (-\sin \phi_{\mathbf{k}}(\mathbf{r}) + \sin(2\mathbf{k} \cdot \mathbf{r} + \phi_{\mathbf{k}}(\mathbf{r}))) \end{aligned} \quad (5)$$

Applying a low pass filter removes the high frequency contributions $\cos(2\mathbf{k} \cdot \mathbf{r} + \phi_{\mathbf{k}})$ and $\sin(2\mathbf{k} \cdot \mathbf{r} + \phi_{\mathbf{k}})$, leaving

$$\begin{aligned} \tilde{X}(\mathbf{r}) &= |I_{\mathbf{k}}(\mathbf{r})| \cos \phi_{\mathbf{k}}(\mathbf{r}) \\ \tilde{Y}(\mathbf{r}) &= -|I_{\mathbf{k}}(\mathbf{r})| \sin \phi_{\mathbf{k}}(\mathbf{r}) \end{aligned} \quad (6)$$

Modulations at frequencies significantly higher than the characteristic (super)lattice periodicity are not expected to have

significant physical meaning and can therefore be removed without affecting interpretability of the data.

The phase is thus given by

$$\phi_{\mathbf{k}}(\mathbf{r}) = \arctan[-\tilde{Y}(\mathbf{r})/\tilde{X}(\mathbf{r})]. \quad (7)$$

It is important to note the real-space coarsening inherent to this approach due to the low-pass filtering step applied between equations (5) and (6). The size of the Gaussian mask around the $\pm\mathbf{k}$ points will dictate the real-space coarsening length and must be chosen judiciously to optimize both the spatial resolution as well as the SNR of the resulting coarse-grained phase field (see Supplementary Fig. S1; Hýtch, 1997).

The resulting 2D phase map of wavevector \mathbf{k} can further provide the “strain” (Hýtch et al., 2003), $\varepsilon_{\mathbf{k}\mathbf{s}}$, along a particular direction \mathbf{s} , with

$$\varepsilon_{\mathbf{k}\mathbf{s}} = \nabla \phi_{\mathbf{k}} \cdot \frac{\mathbf{s}}{|\mathbf{s}|}. \quad (8)$$

For crystallographic analysis, the most common choices of \mathbf{s} will be perpendicular (shear or transverse strain) or parallel (compressive/tensile or longitudinal strain) to \mathbf{k} (note that strains are calculated relative to each \mathbf{k}_i independently of its relative orientation to any other \mathbf{k}_j). Respective to these cases, here we denote all strain maps as either ε_{\perp} or ε_{\parallel} for the sake of clarity. The corresponding \mathbf{k} for each strain map should be clear from its placement in the figure. In certain systems, the “strain” calculated in this way can provide a direct measurement of crystalline displacements or stress response, as described in Hýtch et al.

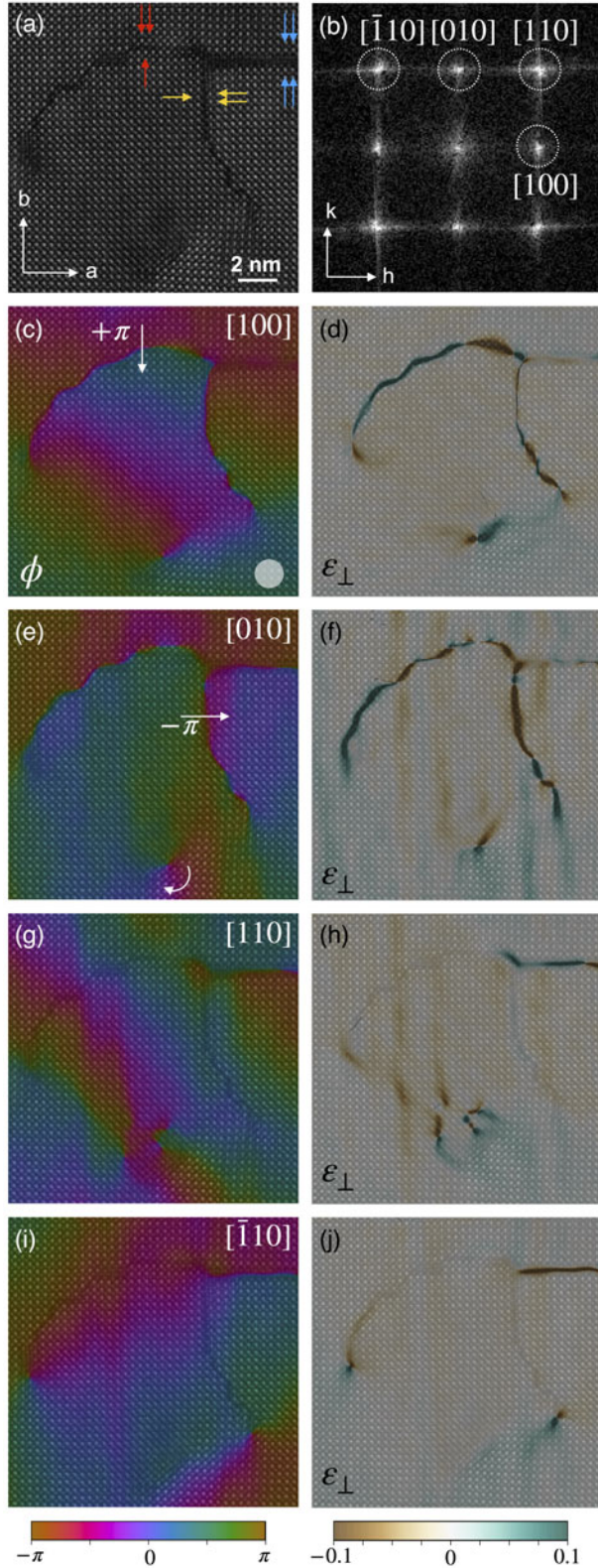


Fig. 2. A complicated, extended crystalline defect in a plan-view SrTiO₃ thin film. Ruddlesden-Popper-type antiphase faults highlighted by red (yellow) arrows in (a) the HAADF-STEM image appear as $+\pi$ ($-\pi$) boundaries in the (c) [100] ((e) [010]) phase and (d,f) corresponding transverse strain ϵ_{\perp} maps. (g–j) The [110] and $[\bar{1}\bar{1}0]$ maps are largely insensitive to the diagonal antiphase faults, instead highlighting compound edge dislocations which can be identified by phase winding and strain singularities even where the structure can not be easily discerned in the HAADF-STEM image. The circle in (c) shows the real-space coarsening length of the lock-in analysis in all maps.

(2003). In more complex or compound systems, however, it is important to make the distinction between modulations in the atomic structure and modulations to a particular set of fringes described by a particular wavevector \mathbf{k} (Peters et al., 2015). For simplicity, we retain the nomenclature of “strain maps” throughout this work, though we note the importance of this distinction for meaningful physical interpretation based upon this or any other Fourier-based technique.

Results and Discussion

Dislocation

A basic demonstration of the phase lock-in analysis technique is presented in Figure 1. A single edge dislocation in Figure 1a with Burgers vector $\mathbf{b} = [100]$ (using the pseudocubic lattice vectors shown) is identified by eye in an otherwise crystallographically clean region of a (La,Ca)MnO₃ membrane. Depending on the set of Bragg peaks used for phase lock-in analysis, the local phase varies as expected across the field of view. When a \mathbf{k} -vector along the same direction of the Burgers vector is used (in this case the [100] peak shown in Figure 1b), a near-perfect 2π phase winding around the edge dislocation clearly emerges, as shown in Figure 1c. The white arrow denotes the direction of the phase winding; an equivalent analysis of the $[\bar{1}00]$ peak would produce an identical but opposite phase map, with the direction of winding reversed (see Supplementary Fig. S3). This reversal is expected when choosing the $-\mathbf{k}$ peak for lock-in analysis, as it will impact the result only through the inverted reference signal $\sin(-\mathbf{k} \cdot \mathbf{r}) = -\sin(\mathbf{k} \cdot \mathbf{r})$ (the cosine signal is even and therefore unchanged). The filtered image amplitude given by equation (3) is already generated from masking both $\pm\mathbf{k}$ peaks, so the $\cos(\mathbf{k} \cdot \mathbf{r} + \phi_{\mathbf{k}})$ terms are also unchanged for the consideration of $-\mathbf{k}$.

The corresponding strain maps in Figures 1e and 1g are consistent with the elastic profiles of a crystalline edge dislocation. Figures 1e and 1g show the transverse strain, ϵ_{\perp} , and longitudinal strain, ϵ_{\parallel} , associated with the dislocation, respectively. The dipole-shaped strain profiles are consistent with those predicted from elastic theory (Hýtch et al., 2003) and are independent of the sign of the peak (i.e., strain profiles for [100] and $[\bar{1}00]$ peaks are equivalent). When \mathbf{k} is orthogonal to \mathbf{b} (in this case the [010] peak), there is very little variation in the phase (Fig. 1d), and the corresponding strain maps remain mostly flat (Figs. 1f and 1h, Supplementary Fig. S2). Both of these results are consistent with expectation: the edge dislocation affects lattice fringes only along the direction of the corresponding Burgers vector \mathbf{b} . Phase mapping of an arbitrary \mathbf{k} will therefore map the effects of the dislocation as a projection of \mathbf{b} onto \mathbf{k} . Given the pseudocubic structure of this (La,Ca)MnO₃ crystal, the [010] peak is orthogonal to the [100] Burgers vector direction, so the projection of \mathbf{b} onto $\mathbf{k} = [010]$ is zero and the resulting maps are essentially featureless. If an intermediate \mathbf{k} is chosen, such as the [110] peak, the 2π phase winding and gradient singularities will again emerge with directional skews (see Supplementary Fig. S4) resulting from the projection of fringes along the [100] direction onto the [110] direction. In this image, identifying the edge dislocation position and direction is trivial even without this or similar phase analysis techniques (Hýtch et al., 2003).

Compound Defect

The same analysis can also be extended to more complicated structures such as the branching defect shown in Figure 2 of a

SrTiO₃ thin film imaged in plan view. In the top left and bottom branches of the defect, close visual inspection of the HAADF-STEM image reveals Ruddlesden-Popper-type out-of-phase boundaries where the fringes of Sr (and Ti) sites shift by approximately half a unit cell on either side of the fault, as highlighted by the red and yellow arrows in Figure 2a. These $\frac{a}{2}$ [110] faults are revealed as $\pm\pi$ phase slips in the lock-in maps of the [100] and [010] \mathbf{k} -vectors, respectively, and ribbons of very high transverse (shear) strains ϵ_{\perp} . The faults appear with essentially equal strength in both sets of maps because the $\frac{a}{2}$ [110] lattice shift has equivalent projections onto the [100] and [010] directions, in contrast to the case of the edge dislocation discussed above.

The right branch of the defect is visibly quite obvious in the HAADF-STEM image, but appears with much weaker contrast in the [010] and especially the [100] phase and strain maps. Close inspection of the HAADF-STEM image reveals why: the Sr (and Ti) atomic fringes remain aligned on either side of the defect, as highlighted by the blue arrows in Figure 2a. The defect thus results in no interruption to crystalline periodicity in the [100] direction, reflected by the flat [100] phase and strain maps. In the [010] direction, a $\sim 3\pi/4$ phase slip and small transverse strain ϵ_{\perp} can be observed, suggesting that the total separation between terminal horizontal atomic rows on either side of the defect is a non-integer value of the lattice constant a .

Compared to the [100] and [010] Bragg peak maps, the phase lock-in analysis of the [110] and $\bar{1}10$ peaks are insensitive to the Ruddlesden-Popper-type $\frac{a}{2}$ [110] faults because they preserve the periodicity of the lattice along those diagonal directions. They do, however, clearly highlight the $\frac{3a}{4}$ [010] lattice slip in the right branch of the defect due to its non-zero projection. In other regions, the resulting structure is more complicated and there is insufficient atomic contrast within the defect to clearly make out the precise structure by eye. Phase lock-in analysis on the [110] and $\bar{1}10$ peaks, however, reveals several distinct edge-type dislocations, each identified by a 2π phase winding and corresponding strain dumbbell singularity. This illustration demonstrates the ability of the phase lock-in analysis to disentangle individual crystalline defect components from more complicated compound structures.

Antipolar Lattice Displacements

While structural defects such as edge dislocations are easily seen in the data, many of the novel or exotic behaviors in complex materials are tied to more subtle lattice effects that may not be immediately apparent even in very high-resolution images. Instead, these phenomena may be revealed only through precise quantification of atomic positions or, in the case of periodic order, through extra superlattice peaks in reciprocal space. For example, alternating transverse antipolar displacements of both the A and B sites in (La,Ca)MnO₃, as shown schematically in Figure 3a, give rise to a strong $[1\frac{1}{2}0]$ superlattice peak in reciprocal space, seen clearly in Figure 3b. Despite its clarity in Fourier space, the periodic structural modulation responsible for this peak is not readily visible in the HAADF-STEM image (Fig. 3c) due to the small displacement magnitudes. With pm-precise atom tracking methods (Savitzky et al., 2017; El Baggari et al., 2018, 2021; Xu et al., 2020a) of the $[1\frac{1}{2}0]$ peak, however, the expected antipolar displacements can be directly measured. Real-space mapping of this ordering reveals a slip in the antipolar superlattice (highlighted in the inset of Fig. 3d), where a single atomic stripe of the distortion is damped to zero and the modulations are out-of-phase on either side.

The local phase slip in the antipolar displacements can be mapped via phase lock-in analysis, avoiding complications of atom-tracking. Here, instead of targeting crystalline peaks as in traditional applications of strain analysis, we extract the variations associated with the superlattice. The phase lock-in map of the $[1\frac{1}{2}0]$ superlattice peak shown in Figure 3h immediately highlights a π phase slip in the antipolar displacements, in agreement with the direct atom tracking. At the same time, conventional strain analysis of three primary Bragg peaks shows no lattice defects or significant strain. This approach therefore reveals defects and modulations in superlattice order even as the atomic lattice exhibits no crystallographic defects. A corollary to this statement demonstrates the advantage of the phase lock-in technique when probing these more exotic forms of order: analyzing only crystalline strain will miss independent modulations in the superlattice order. In many cases, such superlattice disorder is entangled with exotic phenomena (Wei et al., 2014); for instance, in the location of phase slips in charge order displacements, competing properties such as ferromagnetism or localized metallicity can materialize (Milward et al., 2005; Yan et al., 2017).

Mesoscopic Analysis of Coexisting Structural Variations

Across various material platforms, long-range elastic interactions can lead to a multiscale hierarchy of emergent phenomena, necessitating studies from atomic to meso-scales. The phase lock-in analysis in these cases can provide a wealth of information about local order and disorder in lattices and superlattices over large length scales. Figure 4a shows an $8,192 \times 8,192$ pixel² ADF-STEM image of the same plan-view (La,Ca)MnO₃ film shown in Figures 1 and 3 spanning a $0.5 \times 0.5 \mu\text{m}^2$ field of view. While the atomic contrast of the image is not suitable for high-precision quantitative structural analysis such as the atom tracking used in Figure 3d, the pixel size is small enough (~ 8 – 10 pixels per unit cell) to preserve atomic resolution even across such a large area. The periodic information of the image is preserved and the FFT (not shown) contains the same characteristic peaks as those in Figure 3b. Harnessing the robustness of reciprocal space, the phase lock-in technique overcomes the reduced sampling and SNR of a very large field-of-view STEM image to reveal spatial modulations across several order parameters and length scales. Figures 4b and 4c show phase maps tracking the [100] Bragg and $[1\frac{1}{2}0]$ superlattice peaks over the entire field of view. The black-outlined insets show where a 2π phase winding observed in the [100] phase map highlights a simple crystalline edge dislocation, exactly as described in Figure 1. Upon close inspection, the [100] Burgers vector can in fact be traced directly in the original ADF image, as shown in the inset. Remarkably, no disruption to the $[1\frac{1}{2}0]$ superlattice ordering is observed in the same region, demonstrating the independence of the crystalline and superlattice order. Conversely, the white rectangles in Figures 4a–4c mark the regions magnified in 4d–4f, showing a π phase slip in the $[1\frac{1}{2}0]$ superlattice even while the ADF image and flat [100] phase map confirm the perfection of the crystal. The same effect is also observed and discussed in more detail in Figure 3. The phase lock-in analysis method thus enables the atomic-scale analysis of subtle structural distortions for much lower image pixel densities than other high-precision techniques. The large field of view shown here contains several other variations in lattice and superlattice which can be similarly analyzed for an even richer exploration. Clearly, the underlying atomic lattice and emergent order parameters exhibit distinct behaviors.

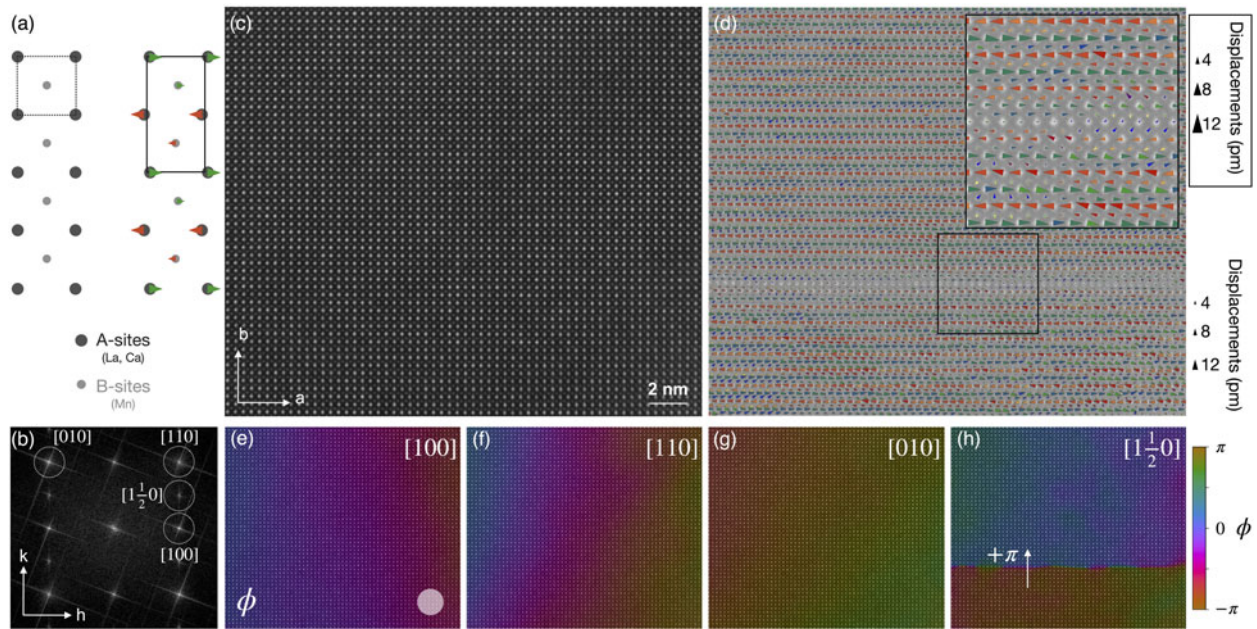


Fig. 3. The ability to lock-in to any \mathbf{k} allows the selection of an emergent peak. (a) The unit cell of an undistorted square perovskite lattice (left, dashed square) doubles along one lattice vector with antipolar A- and B-site displacements which appear in projection as alternating rows of side-to-side atomic displacements (right, solid rectangle). Schematic atomic displacements are exaggerated for clarity and overlaid with arrows depicting the direction and relative magnitude. (b) A corresponding $[1 \frac{1}{2} 0]$ superlattice peak is visible in the FFT of (c) a crystallographically “perfect” region of $(\text{La,Ca})\text{MnO}_3$. (d) Real-space pm-precise atom tracking of the $[1 \frac{1}{2} 0]$ superlattice peak can directly measure the antipolar displacement deviations from the undistorted structure, revealing an antiphase boundary in the superlattice (inset). (e–g) Phase lock-in analysis using any of the primary Bragg peaks ($[100]$, $[010]$, $[110]$, etc.) yields essentially flat phase maps, as expected for an uninterrupted crystalline lattice. (h) When the $[1 \frac{1}{2} 0]$ superlattice peak is used, however, the same boundary in (d) is revealed by a π phase shift in the antipolar displacement order parameter. The circle in (e) shows the real-space coarsening length of the lock-in analysis in all maps.

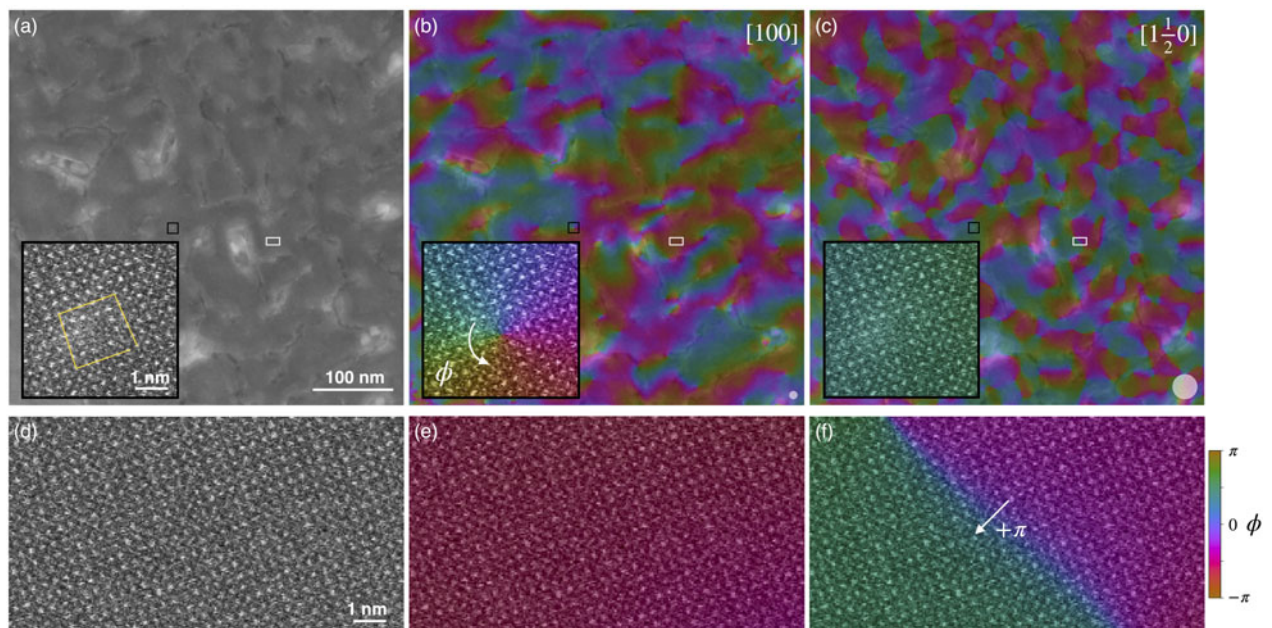


Fig. 4. Relying only on reciprocal-space information rather than Gaussian fitting of atomic positions, the lock-in method enables detailed analysis over large fields of view. (a) An $8,192 \times 8,192$ pixel² ADF-STEM image covering $0.5 \times 0.5 \mu\text{m}^2$ has sufficient pixel density to maintain atomic resolution in plan view images of $(\text{La,Ca})\text{MnO}_3$, allowing the extraction of local lattice information across “global” fields of view by the phase lock-in analysis of different peaks, such as the (b) $[100]$ Bragg peak and (c) $[1 \frac{1}{2} 0]$ superlattice peak discussed in Figure 3. The insets show magnified sections from the ADF-STEM image corresponding to the selected area marked by black boxes where an edge dislocation traced directly on the atomic lattice is highlighted by a 2π winding in the phase of the $[110]$ Bragg peak (as illustrated in Fig. 1). At the same location, no disruption to the $[1 \frac{1}{2} 0]$ superlattice ordering is observed. (d–f) In another region of the membrane marked by the white boxes in (a–c), a phase slip in the superlattice order is revealed by the $[1 \frac{1}{2} 0]$ phase map in an otherwise clean region, as discussed in Figure 3. This form of analysis over very large fields of view can be employed for tracking the mesoscopic interactions and evolution of structural order parameters. The circles in (b) and (c) show the real-space coarsening length of the lock-in analysis of each map.

This mapping capability is limited mostly by the maximum pixel dimensions in commercial instruments: for STEM imaging, increasing the image dimensions through custom or improved scan settings would further expand the accessible fields of view, while applicability to TEM imaging will be limited by the pixel dimensions of detector. As demonstrated here, the application of phase lock-in analysis to large field-of-view S/TEM data provides an avenue to disentangle and explore the interactions between these phenomena mesoscopically.

Compared to conventional strain mapping approaches which can miss the subtleties of superlattice order, the phase lock-in method used here has several advantages. By treating individual components as signals to be demodulated independently, phase lock-in analysis reveals not only conventional defects in the crystalline lattice but also subtle phenomena associated with superlattice order in complex materials. Although crystallographic defects can pin emergent states in certain situations, this is not always the case (as shown here). For instance, an antipolar superlattice can exhibit phase slips which are not directly tied to the location of crystallographic defects. Indeed, many emergent phenomena, such as ferroelectric polarization or charge ordering, exhibit intrinsic modulations tied to their energy scales rather than any crystalline features (Savitzky et al., 2017). Understanding the complexities of these systems thus requires an approach that can directly target the relevant order parameter. Other methods of precise atom-tracking can be similarly sensitive to such modulations, but phase-based image analysis techniques offer the additional advantage of visualizing these responses over multiple length scales. In systems with competing micro- and mesoscopic behaviors, understanding the interplay between multiple orders requires the ability to simultaneously probe picometer- to Ångström-scale distortions across areas spanning nanometers to microns.

Conclusion

The phase lock-in analysis described here and the extension of phase analysis to different Fourier components present a powerful method to disentangle distinct types of order and disorder in STEM images of crystalline materials. At the lattice scale, this method can be used to clearly visualize and distinguish between different types of crystalline defects. As in other methods of GPA, a simple edge dislocation, for example, is highlighted by a distinct 2π winding in the relevant phase map. Ruddlesden-Popper or antiphase-type boundaries, on the other hand, show π phase slips in the direction normal to the boundary plane. More complicated defects are reflected by combinations of these and other characteristic phase responses. The utility of phase analysis techniques for many quantum material systems can, however, be extended further than conventional strain mapping. Beyond the primary lattice, phase lock-in analysis of superlattice peaks also reveals variations in emergent order parameters which are not necessarily tied to crystalline disorder. Analyzing the phase of antipolar displacements in a manganite membrane, for instance, reveals a phase slip in the superlattice even where the underlying atomic structure is pristine. Compared to atom-tracking and other high-precision techniques which may also be sensitive to such distortions, geometric phase analysis by GPA or the phase lock-in method presented here can be more robustly extended to very large fields of view, enabling characterization spanning from the nano- to the micro-scale. The insights provided by such methods will enable a direct visualization of the

interplay between coexisting order parameters and provide new insights into the multiscale hierarchies of emergent phenomena in complex materials.

Supplementary material. To view supplementary material for this article, please visit <https://doi.org/10.1017/S1431927622000125>.

Acknowledgments. We thank Michelle Smeaton, Noah Schnitzer, Elisabeth Bianco, Benjamin H. Savitzky, and Erin E. Fleck for useful discussions about the functionality of phase lock-in analysis. We found the TEMMETA python implementation of GPA developed by Niels Cautaerts (<https://pypi.org/project/temmeta/>, doi:10.5281/zenodo.5205636) helpful for comparison of GPA and phase lock-in analysis techniques.

Financial support. This work was primarily supported by the National Sciences Foundation (Platform for the Accelerated Realization, Analysis, and Discovery of Interface Materials (PARADIM)) under Cooperative Agreement No. DMR-2039380. We acknowledge additional support by the Department of Defense Air Force Office of Scientific Research (No. FA 9550-16-1-0305) and the Packard Foundation. This work made use of the Cornell Center for Materials Research (CCMR) Shared Facilities, which are supported through the NSF MRSEC Program (No. DMR-1719875). The FEI Titan Themis 300 was acquired through No. NSF-MRI-1429155, with additional support from Cornell University, the Weill Institute, and the Kavli Institute at Cornell. The work at SLAC/Stanford is supported by the US Department of Energy, Office of Basic Energy Sciences, Division of Materials Sciences and Engineering, under contract number DE-AC02-76SF00515; and the Gordon and Betty Moore Foundation's Emergent Phenomena in Quantum Systems Initiative through grant number GBMF9072 (synthesis equipment).

Conflict of interest. The authors declare no conflict of interest.

References

- Ahn C, Rabe K & Triscone JM (2004). Ferroelectricity at the nanoscale: Local polarization in oxide thin films and heterostructures. *Science* **303**, 488–491.
- Catalan G, Lubk A, Vlooswijk A, Snoeck E, Magen C, Janssens A, Rispens G, Rijnders G, Blank DH & Noheda B (2011). Flexoelectric rotation of polarization in ferroelectric thin films. *Nat Mater* **10**, 963–967.
- Catalano S, Gibert M, Fowlie J, Iniguez J, Triscone JM & Kreisel J (2018). Rare-earth nickelates RNiO₃: Thin films and heterostructures. *Rep Prog Phys* **81**, 046501.
- Chu MW, Szafraniak I, Scholz R, Harnagea C, Hesse D, Alexe M & Gösele U (2004). Impact of misfit dislocations on the polarization instability of epitaxial nanostructured ferroelectric perovskites. *Nat Mater* **3**, 87–90.
- El Baggari I, Baek DJ, Zachman MJ, Lu D, Hikita Y, Hwang HY, Nowadnick EA & Kourkoutis LF (2021). Charge order textures induced by non-linear couplings in a half-doped manganite. *Nat Commun* **12**, 3747.
- El Baggari I, Savitzky BH, Admasu AS, Kim J, Cheong SW, Hovden R & Kourkoutis LF (2018). Nature and evolution of incommensurate charge order in manganites visualized with cryogenic scanning transmission electron microscopy. *Proc Natl Acad Sci USA* **115**, 1445–1450.
- Fan Z, Ma T, Wei J, Yang T, Zhou L & Tan X (2020). TEM investigation of the domain structure in PbHfO₃ and PbZrO₃ antiferroelectric perovskites. *J Mater Sci* **55**, 4953–4961.
- Findlay S, Shibata N, Sawada H, Okunishi E, Kondo Y, Yamamoto T & Ikuhara Y (2009). Robust atomic resolution imaging of light elements using scanning transmission electron microscopy. *Appl Phys Lett* **95**, 191913.
- Gao P, Kumamoto A, Ishikawa R, Lugg N, Shibata N & Ikuhara Y (2018). Picometer-scale atom position analysis in annular bright-field STEM imaging. *Ultramicroscopy* **184**, 177–187.
- Gao P, Liu HJ, Huang YL, Chu YH, Ishikawa R, Feng B, Jiang Y, Shibata N, Wang EG & Ikuhara Y (2016). Atomic mechanism of polarization-controlled surface reconstruction in ferroelectric thin films. *Nat Commun* **7**, 11318.
- Guo H, Wang Z, Dong S, Ghosh S, Saghaezhian M, Chen L, Weng Y, Herklotz A, Ward TZ, Jin R, Pantelides ST, Zhu Y, Zhang J & Plummer EW (2017). Interface-induced multiferroism by design in complex oxide superlattices. *Proc Natl Acad Sci USA* **114**, E5062–E5069.

- Han Y, Li MY, Jung GS, Marsalis MA, Qin Z, Buehler MJ, Li LJ & Muller DA (2018). Sub-nanometre channels embedded in two-dimensional materials. *Nat Mater* **17**, 129–133.
- Hong SS, Gu M, Verma M, Harbola V, Wang BY, Lu D, Vailionis A, Hikita Y, Pentcheva R, Rondinelli JM & Hwang HY (2020). Extreme tensile strain states in $\text{La}_{0.7}\text{Ca}_{0.3}\text{MnO}_3$ membranes. *Science* **368**, 71–76.
- Hwang J, Zhang JY, D'Alfonso AJ, Allen LJ & Stemmer S (2013). Three-dimensional imaging of individual dopant atoms in SrTiO_3 . *Phys Rev Lett* **111**, 266101.
- Hýtch M & Gandais M (1995). Quantitative criteria for the detection and characterization of nanocrystals from high-resolution electron microscopy images. *Philos Mag A* **72**, 619–634.
- Hýtch M, Snoeck E & Kilaas R (1998). Quantitative measurement of displacement and strain fields from HREM micrographs. *Ultramicroscopy* **74**, 131–146.
- Hýtch MJ (1997). Analysis of variations in structure from high resolution electron microscope images by combining real space and fourier space information. *Microsc Microanal Microstruct* **8**, 41–57.
- Hýtch MJ, Putaux JL & Pénisson JM (2003). Measurement of the displacement field of dislocations to 0.03 \AA by electron microscopy. *Nature* **423**, 270–273.
- Jia CL, Nagarajan V, He JQ, Houben L, Zhao T, Ramesh R, Urban K & Waser R (2007). Unit-cell scale mapping of ferroelectricity and tetragonality in epitaxial ultrathin ferroelectric films. *Nat Mater* **6**, 64–69.
- Kim H, Zhang JY, Raghavan S & Stemmer S (2016). Direct observation of Sr vacancies in SrTiO_3 by quantitative scanning transmission electron microscopy. *Phys Rev X* **6**, 041063.
- Lawler MJ, Fujita K, Lee J, Schmidt AR, Kohsaka Y, Kim CK, Eisaki H, Uchida S, Davis JC, Sethna JP & Kim Ea. (2010). Intra-unit-cell electronic nematicity of the high- T_c copper-oxide pseudogap states. *Nature* **466**, 347–351.
- Lazić I, Bosch EGT & Lazar S (2016). Phase contrast STEM for thin samples: Integrated differential phase contrast. *Ultramicroscopy* **160**, 265–280.
- LeBeau JM, Findlay SD, Allen LJ & Stemmer S (2008). Quantitative atomic resolution scanning transmission electron microscopy. *Phys Rev Lett* **100**, 206101.
- Liao Z, Sun W, Zhang Q, Li JF & Zhu J (2019). Microscopic origin of the high piezoelectric response of Sm-doped BiFeO_3 near the morphotropic phase boundary. *J Appl Phys* **125**, 175113.
- Loudon JC, Kourkoutis LF, Ahn JS, Zhang CL, Cheong SW & Muller DA (2007). Valence changes and structural distortions in "charge ordered" manganites quantified by atomic-scale scanning transmission electron microscopy. *Phys Rev Lett* **99**, 237205.
- Lu D, Baek DJ, Hong SS, Kourkoutis LF, Hikita Y & Hwang HY (2016). Synthesis of freestanding single-crystal perovskite films and heterostructures by etching of sacrificial water-soluble layers. *Nat Mater* **15**, 1255–1260.
- Mesaros A, Fujita K, Eisaki H, Uchida S, Davis J, Sachdev S, Zaenen J, Lawler M & Kim EA (2011). Topological defects coupling smectic modulations to intra-unit-cell nematicity in cuprates. *Science* **333**, 426–430.
- Milward GC, Calderon MJ & Littlewood P (2005). Electronically soft phases in manganites. *Nature* **433**, 607–610.
- Nelson CT, Winchester B, Zhang Y, Kim S-J, Melville A, Adamo C, Folkman CM, Baek S-H, Eom C-B, Schlom DG, Chen L-Q & Pan X (2011). Spontaneous vortex nanodomain arrays at ferroelectric. *Nano Lett* **11**(2), 828–834.
- Nord M, Vullum PE, MacLaren I, Tybell T & Holmestad R (2017). Atomap: A new software tool for the automated analysis of atomic resolution images using two-dimensional gaussian fitting. *Adv Struct Chem Imag* **3**, 9.
- Peters JJP, Beanland R, Alexe M, Cockburn JW, Revin DG, Zhang SY & Sanchez AM (2015). Artefacts in geometric phase analysis of compound materials. *Ultramicroscopy* **157**, 91–97.
- Ramesh R & Spaldin NA (2007). Multiferroics: Progress and prospects in thin films. *Nat Mater* **6**, 21–29.
- Rouviere JL & Sarigiannidou E (2005). Theoretical discussions on the geometrical phase analysis. *Ultramicroscopy* **106**, 1–17.
- Savitzky BH, El I, Clement CB, Waite E, Goodge BH, Baek DJ, Shekelton JP, Pasco C, Nair H, Schreiber NJ, Hoffman J, Admasu AS, Kim J, Cheong Sw., Bhattacharya A, Schlom DG, Mcqueen TM, Hovden R & Kourkoutis LF (2018). Image registration of low signal-to-noise cryo-STEM data. *Ultramicroscopy* **191**, 56–65.
- Savitzky BH, El Baggari I, Admasu AS, Kim J, Cheong SW, Hovden R & Kourkoutis LF (2017). Bending and breaking of stripes in a charge ordered manganite. *Nat Commun* **8**, 1883.
- Spaldin NA & Fiebig M (2005). The renaissance of magnetoelectric multiferroics. *Science* **309**, 391–392.
- Tokura Y & Hwang HY (2008). Complex oxides on fire. *Nat Mater* **7**, 694–695.
- Voyles PM, Grazul JL & Muller DA (2003). Imaging individual atoms inside crystals with ADF-STEM. *Ultramicroscopy* **96**, 251–273.
- Wang Y, Salzberger U, Sigle W, Suyolcu YE & van Aken PA (2016). Oxygen octahedra picker: A software tool to extract quantitative information from STEM images. *Ultramicroscopy* **168**, 46–52.
- Wang Z, Goodge BH, Baek DJ, Zachman MJ, Huang X, Bai X, Brooks CM, Paik H, Mei AB, Brock JD, Maria JP, Kourkoutis LF & Schlom D (2019). Epitaxial SrTiO_3 film on silicon with narrow rocking curve despite huge defect density. *Phys Rev Mater* **3**, 073403.
- Wei XK, Tagantsev AK, Kvasov A, Roleder K, Jia CL & Setter N (2014). Ferroelectric translational antiphase boundaries in nonpolar materials. *Nat Commun* **5**, 3031.
- Xu C, Chen Y, Cai X, Meingast A, Guo X, Wang F, Lin Z, Lo TW, Maunders C, Lazar S, Wang N, Lei D, Chai Y, Zhai T, Luo X & Zhu Y (2020a). Two-dimensional antiferroelectricity in nanostripe-ordered In_2Se_3 . *Phys Rev Lett* **125**, 047601.
- Xu R, Huang J, Barnard ES, Hong SS, Singh P, Wong EK, Jansen T, Harbola V, Xiao J, Wang BY, Crossley S, Lu D, Liu S & Hwang HY (2020b). Strain-induced room-temperature ferroelectricity in SrTiO_3 membranes. *Nat Commun* **11**, 3141.
- Yan S, Iaia D, Morosan E, Fradkin E, Abbamonte P & Madhavan V (2017). Influence of domain walls in the incommensurate charge density wave state of Cu-intercalated $1T\text{-TiSe}_2$. *Phys Rev Lett* **118**, 106405.
- Yankovich AB, Berkels B, Dahmen W, Binev P, Sanchez SI, Bradley SA, Li A, Szlufarska I & Voyles PM (2014). Picometre-precision analysis of scanning transmission electron microscopy images of platinum nanocatalysts. *Nat Commun* **5**, 4155.
- Zheng Q, Schreiber NJ, Zheng H, Yan J, McGuire MA, Mitchell JF, Chi M & Sales BC (2018). Real space visualization of competing phases in $\text{La}_{0.6}\text{Sr}_{2.4}\text{Mn}_2\text{O}_7$ single crystals. *Chem Mater* **30**, 7962–7969.
- Zhu Y, Ophus C, Ciston J & Wang H (2013). Interface lattice displacement measurement to 1 pm by geometric phase analysis on aberration-corrected HAADF STEM images. *Acta Mater* **61**, 5646–5663.